Shen, Y., Freddi, F., Li, J. (2022). Experimental and numerical investigates on seismic behavior of socket connections and hybrid connections for PCFT bridge columns. Engineering Structures, 253: 113833. https://doi.org/10.1016/j.engstruct.2021.113833.

Experimental and numerical investigations of the seismic behavior of socket and hybrid connections for PCFT bridge columns

Yu Shen[a], Fabio Freddi[b], Jianzhong Li[a,*]

[a] *State Key Laboratory of Disaster Reduction in Civil Engineering, Tongji University, Shanghai 200092, China*
[b] *Dept. of Civil, Environmental & Geomatic Engineering, University College of London, London WC1E 6BT, U.K.*
[*]Corresponding Author. Tel.: +86 (21) 65980455. E-mail address: lijianzh@tongji.edu.cn (J. Li)

ABSTRACT

The present paper investigates an innovative seismic-resilient bridge column-footing socket connection (SC) for post-tensioned concrete-filled steel tube (PCFT) columns defined according to the Accelerated Bridge Construction (ABC) requirements. The PCFT-SC column uses an embedded steel tube to dissipate the seismic energy and unbonded post-tensioned (PT) bars to improve the self-centering capacity. Experimental tests were performed on a PCFT-SC column, and the seismic response was compared with the PCFT column with hybrid connection (HC) previously investigated by the authors. The experimental tests confirmed that the PCFT-SC column could develop large strength, stiffness, and ductility capacity and that, compared with the PCFT-HC column, its seismic performance is competitive for drifts up to 2.8%. For larger drifts, the performances are slightly reduced due to the steel tube local buckling and the resulting PT force loss. However, even in these cases, the PCFT-SC column could be preferred due to its constructional advantages. Simplified models of PCFT columns with the SC and HC were developed in OpenSees, including modeling details accounting for the effects of the PT force loss. The numerical results, calibrated against the experimental data, showed the importance of considering PT force loss in the cyclic load analysis for PCFT columns.

Keywords: Bridge column; Concrete-filled steel tube (CFT); Column-footing connections; Unbonded post-tensioning; Cyclic testing; Numerical modeling.

1. Introduction

Traditional seismic design strategies included in current codes [1-5] are based on energy dissipation related to construction damage, often leading to considerable direct (*e.g.,* casualties, repair cost) and indirect (*e.g.,* downtime) losses as a consequence of 'rare' (*i.e.,* high intensity) seismic events. Additionally, the inelastic deformations in the structural components can lead to large residual deformations, thus impairing the repairability of the constructions [6] (*e.g.,* after the Kobe earthquake in Japan, over one hundred Reinforced Concrete (RC) bridges were demolished due to the excessive residual drift). This situation strongly affects the overall resilience of communities in seismic-prone regions, especially when the damaged structures include strategic transportation facilities, such as bridges or tunnels connecting essential services that must remain operational in the aftermath of a damaging earthquake (*e.g.,* hospitals, fire stations, etc.) [7]. At the same time, and independently from the earthquake-induced damages, transportation facilities are subjected to severe aging effects [8], and significant resources are often required for their repair, rehabilitation, and reconstruction. These include time on those construction activities that disrupt the traffic users and local businesses. In this context, one of the main objectives of nowadays transportation industry is to explore alternative design strategies and/or technological solutions for bridge structures that can, from one side, minimize the seismic damage, on the other side, expedite construction and/or reparation time mitigating disruptions to the traveling public.

The present paper investigates innovative seismic-resilient bridge column-footing connections, which are based on the Accelerated Bridge Construction (ABC) requirements [9] and combine the benefits of rocking systems, unbonded post-tensioned (PT) bars, and energy dissipation (ED) components. While the PT bars improve the self-centering capability, the ED components aim to increase the structure's dissipation capacity [10-13].

Rocking columns are typically expected to experience minimal damage during severe seismic events [14-16]. However, it has been demonstrated that, if not properly detailed, RC rocking columns may be subjected to local damage at the contact surface with the foundation due to the additional compression force caused by the post-tensioning [12,17-20]. To overcome this drawback, recent research studies investigated solutions aiming to enhance the column shaft's integrity. These solutions include the use of high-performance concrete [21,22], fiber-reinforced polymer wraps [19,23], or steel tubes [11,17,24-26]. Among these strategies, the use of steel tubes to encase the RC column, *i.e.,* concrete-filled steel tube (CFT) column, is considered in the present study as a simple and practical solution with multiple benefits: from one hand, it increases the confinement of the concrete, on the other hand, the steel tube act as formwork for casting [11,25,27] enabling a fast construction. In particular, it avoids the need for reinforcing cages, shoring, and temporary formwork, promoting the ABC objectives.

The benefits of using post-tensioned concrete-filled steel tube (PCFT) columns coupling the features of PT connections and CFT columns have been demonstrated in several studies. Among others, Chou *et al.* [24,28] and Guerrini *et al.* [25,29] conducted cyclic tests and numerical investigation on the PT precast CFT segment columns and PT dual-shell CFT columns, respectively. Similarly, Tobolski [30] tested two PCFT column-bent cap subassemblies, one column

encased by a full-height steel shell and the other sandwiched by two concentric steel shells. These research studies showed that this type of column connection exhibits satisfactory seismic performances even after large inelastic drifts. However, these studies also indicated that the mortar bed at the column ends is susceptible to crushing and represents the weakest part of the system [25,30]. To overcome this issue, Shen *et al.* [11] experimentally investigated the seismic performance of a PCFT column with hybrid connection (HC) with ultra-high-performance concrete (UHPC) as mortar bed.

According to the recommendation of Shen *et al.* [11] and inspired by the embedded ring CFT connections developed by Stephens *et al.* [27,31,32] and Leman *et al.* [33], the ED bars can be substituted by steel shell extended into the footing of the connection with sufficient embedment length. This solution represents a more practical configuration for 'real-life' applications [27] and, although the rocking behavior at the base interface is precluded, the inclusion of PT bars is still beneficial for the column's self-centering capacity. This base connection is a refinement of the conventional emulative socket connection (SC) formed by embedding the precast CFT column into a preformed void of a precast foundation where grout is poured to fill the void [9,34]. Based on the results of relevant research studies on bridge columns with SC [32,34-38], the seismic performance is comparable to that of a cast-in-place system if the embedded length is adequate. Thus, it is expected that the PCFT designed with SC (PCFT-SC), *i.e.*, where PT bars provide the self-centering capacity and the embedding steel tube is used as the ED component, may achieve the desired seismic performance.

The present study experimentally and numerically investigates a PCFT-SC column and compares the results with a PCFT-HC column previously tested by the authors [11]. The specimen dimensions, material properties, key design parameters, and test protocols for both configurations are almost identical, allowing the comparison of the seismic performance between the two columns. Based on the test observations and results, the finite element (FE) models, which incorporate the effects of PT force loss and boundary condition of base connections, are developed and validated for both PCFT bridge column types.

2. Post-tensioned concrete-filled steel tube (PCFT) column specimens

The experimental test specimen consists of a 1/4.75-scale precast bridge PCFT-SC column. This is consistent with the previous test campaign on PCFT-HC columns conducted by the authors [11]. The overall dimensions of the specimens and the details of both base connections are shown in Fig. 1, while Table 1 summarizes the main design parameters. The test of the PCFT-SC column was conducted with the same post-tensioning force and cyclic loads history used for the PCFT-HC column identified as *'specimen PCFT-10-3.6'* in the previous experimental campaign [11], where 10 and 3.6 represent the initial PT force ratio and the ED reinforcement ratio (*i.e.*, 10% and 3.6%), respectively. The geometry of both specimens is shown in Fig. 1(a). The height measured from the column base section to the location of application of the lateral load was 2000 mm, and the section depth was 440 mm, giving an aspect ratio of 4.55. A vertical 70-mm-diameter PVC duct allowed a 50-mm-diameter high-strength PT bar to run through the specimens, which produced a total unbonded length of 2700 mm for the threaded bar. The anchorage systems for the PT bars were comprised of bearing plates and anchor nuts. The bars were anchored in footings and extended to the pier caps, as shown in Fig. 1(a). It is worth highlighting that the anchorage of these bars on the bridge caps can be inspected at any time, during and after construction, also allowing the re-tensioning when PT loss occurs after severe earthquakes. In this study, the PT bar had a nominal yield strength, f_{y_pt}, of 930 MPa and was designed to behave elastically during the tests to ensure the self-centering capability of the columns. The footing and cap beam were scaled from the prototype bridge pier to have dimensions of 1.76×1.16×0.60 m and 2.20×0.74×0.50 m, respectively, and designed according to the capacity design rules to avoid any damage of these components during the experimental test [1,31]. A square hole of 0.20×0.20×0.15 m at the footing block allowed the anchorage of the PT bar at the bottom end.

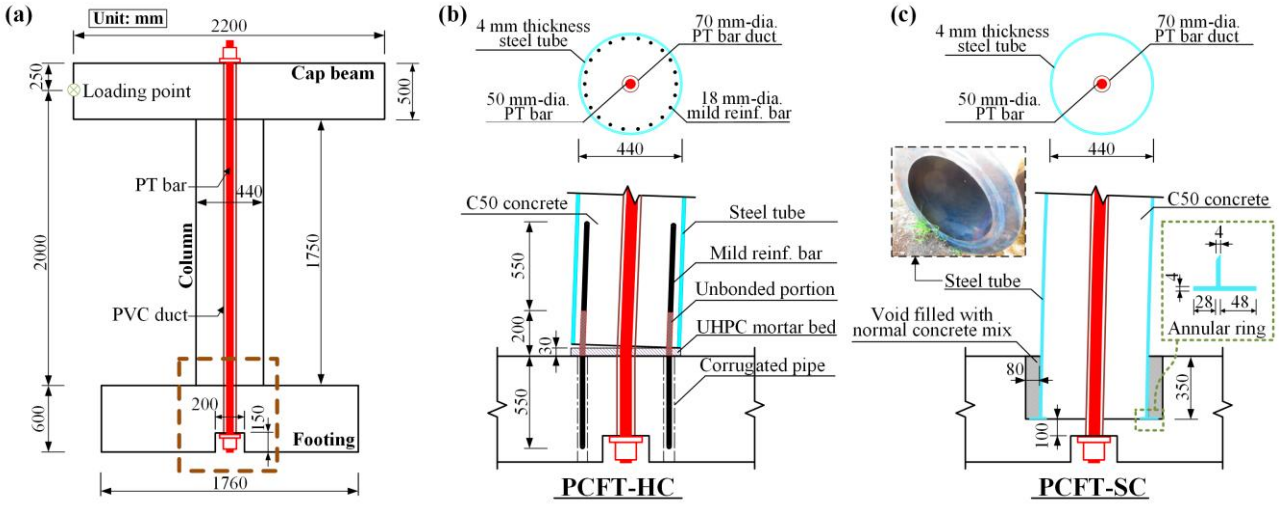

Fig. 1. Summary of test columns: (a) Specimens dimensions, (b) PCFT column with hybrid connection (PCFT-HC), and (c) PCFT column with socket connection (PCFT-SC).

Table 1 Test specimen design parameters.

Specimen	Column material	Connection	ED bars	ρ_{ED} (%)	ρ_{ST} (%)	ρ_{Sum} (%)
PCFT-HC	CFT	HC	22-D18	3.6	0	3.6
PCFT-SC	CFT	SC	No bars	0	3.6	3.6

Notes: D18 refers to the diameter of 18 mm; ρ_{ED} and ρ_{ST} are the steel ratio of longitudinal ED bars and steel tube, respectively, which are extended into the footing; and ρ_{Sum} represents the sum of ρ_{ED} and ρ_{ST}.

2.1 PCFT column with hybrid connection (PCFT-HC)

The PCFT-HC column was developed with a combination of CFT column and controlled rocking (Fig. 1(b)). A natural rocking interface emerged at the column base under seismic loading. This characteristic is beneficial to the seismic performance of the PCFT-HC system because the rocking mechanism allows accommodating the column displacements in all directions, concentrates the inelastic deformations in the ED bars, and the combination of the rocking mechanism and PT bars provides the self-centering capability of the system.

The design strategy of the PCFT-HC for a specified target drift (assumed as 5% in the present study) aims at meeting the following design objectives: *(1)* minimum steel tube thickness; *(2)* prevention of PT bar yielding; *(3)* sufficient ED and, (4) self-centering capability. Considering the large axial compression force (post-tensioning and gravity) imposed on the PCFT-HC, the thickness and strength of the steel tube should satisfy Eq. (1) by following the recommendations of the GB 50936-2014 Code [39].

$$D/t \le 135\frac{235}{f_{y\_st}} \tag{1}$$

where D, t, and f_{y_st} are respectively the diameter, thickness, and the yielding strength of the steel tube. Also, at the target drift, the strain of the steel tube should be lower than the steel yielding threshold to preserve confinement for the inner concrete. The initial PT force was selected to prevent the yielding of the PT bar at the target drift according to the following Eq. (2):

$$\sigma_{PT} = \sigma_{PT0} + E_{PT}\frac{\Delta_{PT}}{L_{PT}} \le f_{y\_pt} \tag{2}$$

where σ_{PT} and σ_{PT0} are respectively the stresses in PT tendon at the target drift and the initial state; E_{PT} and L_{PT} are respectively the elastic modulus and the unbonded length of PT bar; and Δ_{PT} is the elongation of PT bar at the target drift, which can be obtained through rigid body kinematic as specified in the following Eq. (3):

$$\Delta_{PT} = \theta \times (D/2 - c) \tag{3}$$

where θ is the joint rotation corresponding to the target drift; and c is the neutral axis depth from the compressive toe, which is assumed equal to 0.25D based on recommendations in literature [29]. Self-centering and ED capacities in PFCT-HC need to be balanced to meet the design objectives. This balance can be defined according to the self-centering coefficient, Λ_c [25,29] in the following Eq. (4):

$$\Lambda_c = \frac{F_{ED}}{P_u + F_{PT}} \le 1 \tag{4}$$

where F_{ED} is the resisting force provided by the ED; P_u is the gravity force imposed on the column by the superstructure; and F_{PT} is the PT force. The design should ensure Λ_c values lower than 1.0, such that gravity and PT forces are large enough to overcome F_{ED} and hence, able to close the interface gap. However, in addition to the one produced by the ED components, other non-linear mechanisms are usually involved in the system, and conservative Λ_c values are usually adopted.

The selected PCFT-HC reference specimen (*i.e.*, PCFT-10-3.6), shown in Fig. 1(b), included 22 ED bars with a diameter of 18 mm (*i.e.*, reinforcement ratio ρ_{ED} of 3.6%) (Table 1), which were anchored in grouted corrugated pipes at the footing, and debonded for 200 mm above the column-footing interface by wrapping them with foam tape. These ED bars were made of mild steel with a yielding strength of approximately 500 MPa. The CFT column was composed of a 4-mm-thickness circular steel tube with a nominal yielding strength of 235 MPa and concrete with a cubic compressive strength of 56 MPa (*i.e.*, cylinder compressive strength, f_c, of approximately 41 MPa). The footing and cap beam were cast from the same batches of concrete as for the column. The steel tube is placed along the shaft and hence, only provides confinement for the concrete core and does not contribute to the resistance of the column to the rocking motion (*i.e.*, ρ_{ST} = 0%). The PT bar was post-tensioned to 493 kN, corresponding to a force ratio of 0.1 (*i.e.*, the initial PT force divided by the ultimate axial compressive load capacity of the CFT column [40,41]). Additionally, a layer of UHPC mortar bed was placed beneath the CFT column base to level out the surface. More details on the PCFT-HC column can be found in

Shen *et al*. [11]. It is noteworthy that the PCFT-HC reference *'specimen PCFT-10-3.6'* does not satisfy Eq. (4) (*i.e.*, Λ_c = 2.0 > 1.0), and hence a complete self-centering behavior is not expected.

2.2 PCFT column with socket connection (PCFT-SC)

The PCFT-SC featured an emulative unbonded PT variant of the SC (Fig. 1(c)). This PCFT connection concept is similar to the embedded ring connection proposed by Stephens *et al.* [27,31,32], which conducted a series of quasi-static tests and numerical analysis indicating its increased load capacity and promising ductile behavior. However, self-centering details were not incorporated in the previous research studies, and the present work investigates the influence of PT bars on the self-centering capability of the connection.

As shown in Fig. 1(c), a cylinder void with a diameter of 0.6 m was designed in the precast footing, and the CFT column was placed into the void by an overhead crane. After alignment of the column, the gap (of about 8 cm width) between the column shaft and footing was filled with the concrete mix. Finally, a PT bar with material, diameter, and post-tensioning force equivalent to those used for the PCFT-HC was included. Following this fabrication process, the steel tube of the CFT column was used not only to transversely confine concrete but also to provide flexure strength and ED for the column. The design of the PCFT-SC aimed at replicating geometry and materials of the previously investigated PCFT-HC reference *'specimen PCFT-10-3.6'*, hence allowing a fair comparison. A steel tube with the same material, diameter, and thickness as those of the PCFT-HC, corresponding to a steel ratio of ρ_{ST} of 3.6%, was employed in PCFT-SC (Table 1). No longitudinal ED bars were used in the specimen PCFT-SC (*i.e.*, ρ_{ED} = 0%). C50 concrete (*i.e.*, cubic compressive strength of 50 MPa), comparable to the resistance of concrete of the PCFT-HC, was used for the PCFT-SC. It is noteworthy that the concrete mix used for grouting was chosen to be close to that used for the footing. However, the coarse aggregates were precluded in the concrete matrix due to the limited space between the column and footing (*i.e.*, only containing fine aggregates). Thus, the actual cubic compressive strength of grouting concrete was only 34.9 MPa, which did not meet the intent of strength requirements.

To ensure that the column-footing connection would not be the weak link in the PCFT-SC specimen, particular attention was paid to the design and provisions of the SC details. An annular flange was welded to the bottom end of the steel tube to transfer loads from the steel tube and concrete core to the footing [33]. This annular flange was required to prevent anchorage slip between the steel tube and the concrete allowing the development of the full strength moment-resistance of the connection. The detailed dimensions of the annular flange are illustrated in Fig. 1(c). This flange had the same thickness as the steel tube and projected a distance of 12 and 7 times the tube thickness (48 and 28 mm) outside and inside the tube, respectively (see Fig. 1(c)). Thus, the total projection length was equivalent to 19 times the tube thickness, which satisfied the recommendation of 16 times tube thickness by Stephens *et al.* [31]. Additionally, a sufficient embedded depth of the PCFT column should also be provided into the footing. The depth of the void, *i.e.*, the embedded depth of the PCFT column, was designed to be 350 mm (approximately 0.8 times the column diameter) based on the required embedment depth for the CFT column [31]. The dowel detail with the addition of vertical shear friction across the steel tube surface of the embedded portion assured the development of a well-anchored SC connection.

3. Experimental test program

Fig. 2 shows the global experimental setup of the specimen PCFT-SC. The loading protocol and apparatus were almost identical to those of the previous PCFT-HC column test [11]. The PCFT-SC was tested using a reaction frame with a pair of vertical actuators to apply the axial force and a reaction wall with one horizontal actuator to apply the lateral load. The two symmetrical vertical actuators provided a total constant force of 345 kN (*i.e.*, axial compression ratio equaling 7%) on the top of the specimen. During the tests, the vertical actuators were free to move laterally by the slide rail hence maintaining the applied force in the vertical direction (Fig. 2(a)). The cyclic lateral loading protocol used in the previous PCFT-HC test was used for the PCFT-SC. Fig. 3 depicts the detailed cyclic loading history of the PCFT-SC test, including both the force- and drift-controlled histories. The push and pull loads were respectively designated to the loadings from East-to-West and West-to-East. Each loading level was repeated for three complete cycles except for the last loading level (*i.e.*, 6.0% drift), which had only one cycle after which the test was stopped due to the tearing of the steel tube. The test was terminated when the tearing of the steel tube occurred, and load resistance dropped to less than 85% of the peak force accordingly. A total of 49 cycles with 5 force amplitude levels and 12 drift amplitude levels were used throughout the test. The lateral loading was applied at the height of 2 m above the footing, and a string potentiometer was installed at this height to monitor the displacement of the loading point. Other testing response parameters were recorded by various data instrumentations, as shown in Fig. 2(a). Eight linear variable differential transformers (LVDTs), placed on both sides of the columns and at a distance of 120 mm, measured the relative displacements between adjacent column sections. Similarly, six strain-gauge rosettes, placed at a distance of 100 mm, measured the strains of the steel tube. Additionally, the strains of the PT bar were measured by strain gauges, as illustrated in Fig. 2(a). To facilitate recognizing the damage locations, horizontal and vertical marked lines spaced at 5 cm were drawn around the lower half of the column before the test (see Fig. 2(b)).

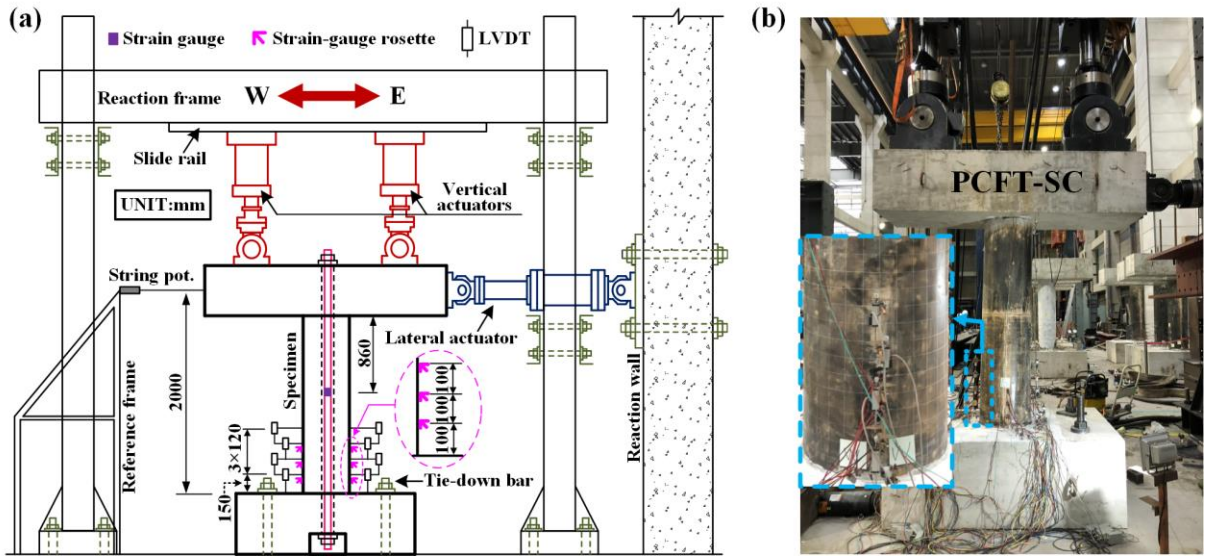

Fig. 2. (a) Representation of the test set-up in elevation, (b) PCFT-SC specimen.

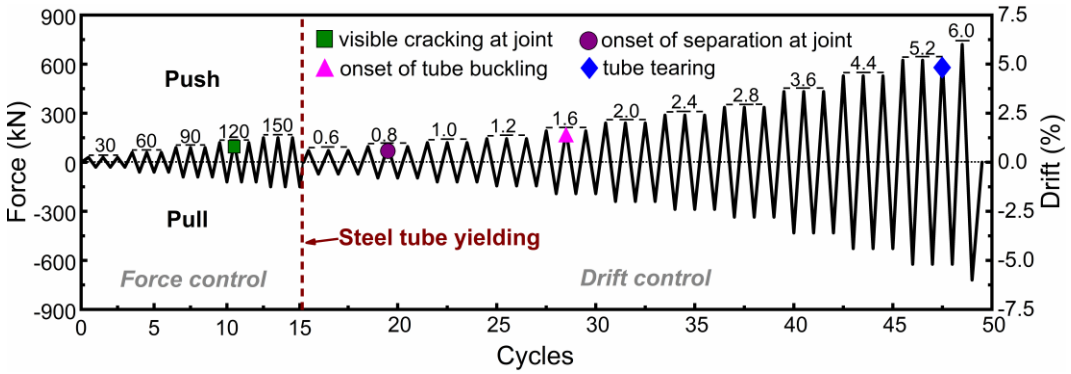

Fig. 3. Cyclic loading history.

4. Experimental test results and discussion

Only the cyclic response and damage progression of the PCFT-SC specimen are presented in detail herein. Conversely, the interested reader can refer to Shen *et al.* [11] for the detailed description and the experimental outcomes of the PCFT-HC. However, some results of the PCFT-HC test are reported in the following for comparison purposes.

4.1 Damage states

Fig. 4 illustrates the key damage states of the column-footing joint for the PCFT-SC specimen during the tests. Before the 0.4% drift (*i.e.*, corresponding to an applied force of 120 kN; square symbol in Fig. 3), a circumferential crack in the concrete at the column-footing joint emerged, and some hairline cracks formed in the surface of the footing along the direction of outward normal to the column (Fig. 4(a)). These cracks only appeared during the peak drifts and closed after each drift level was completed. For increasing drift amplitudes, the circumferential crack progressed, and a separation between the tube and surrounding concrete initiated (circular symbol in Fig. 3), as shown in Fig. 4(b). Meanwhile, the cracks in the concrete footing were propagated to the footing edges but remained local and small. Visible local buckling of the steel tube was first detected for lateral drift of 1.6% (Fig. 4(c); triangle symbol in Fig. 3). This local buckling was developed near the base stub with a height of about 5 cm. After such drift, cracks in the footing ceased further development; however, the local buckling deformation at the column base was progressively more severe, with the apex of the buckle at the height of approximately 3 cm from the base (Fig. 4(d)). With the reversal load, the buckling deformation vanished, and the profile straightened, the gap opening became progressively evident, and an elongation of the steel tube was observed. As shown in Fig. 4(d), for a peak drift of 3.6%, the measured elongation of the steel tube on the East face of the column base was approximately 6 mm. As the cyclic history continued, the process of buckling and straightening of the profile was repeated. For a drift of 5.2%, the buckling of the profile was considerable, and on the third cycle of this drift amplitude, a horizontal tearing occurred at the location of the buckling apex (Fig. 4(e); rhombus symbol in Fig. 3). Furthermore, some pulverized concrete sand spilled out through the fractured cracks, which indicated the crushing of the concrete core. The test terminated after completing the first cycle of 6.0% drift amplitude due to a significant tearing at both sides of the column base (about 35 cm length for each side, Fig. 4(f)) and a drop in the lateral force resistance.

In general, the developed PCFT-SC showed a high load capacity and was able to transfer the loads from the PCFT column to the footing. The footing integrity was kept along with the test with the only exception of a few minor and superficial cracks. Similar to the test observations for the PCFT-HC [11], most damages for PCFT-SC were concentrated at the bottom of the column. However, the damage states of column bottom between them were different. The failure modes for PCFT-SC were related to the buckling and tearing of the steel tube and the crushing of the concrete core, both of which were difficult to repair. For PCFT-HC, the column shaft was sound with some crushing at the edges of the mortar bed and failed because of the fracture of ED bars [11].

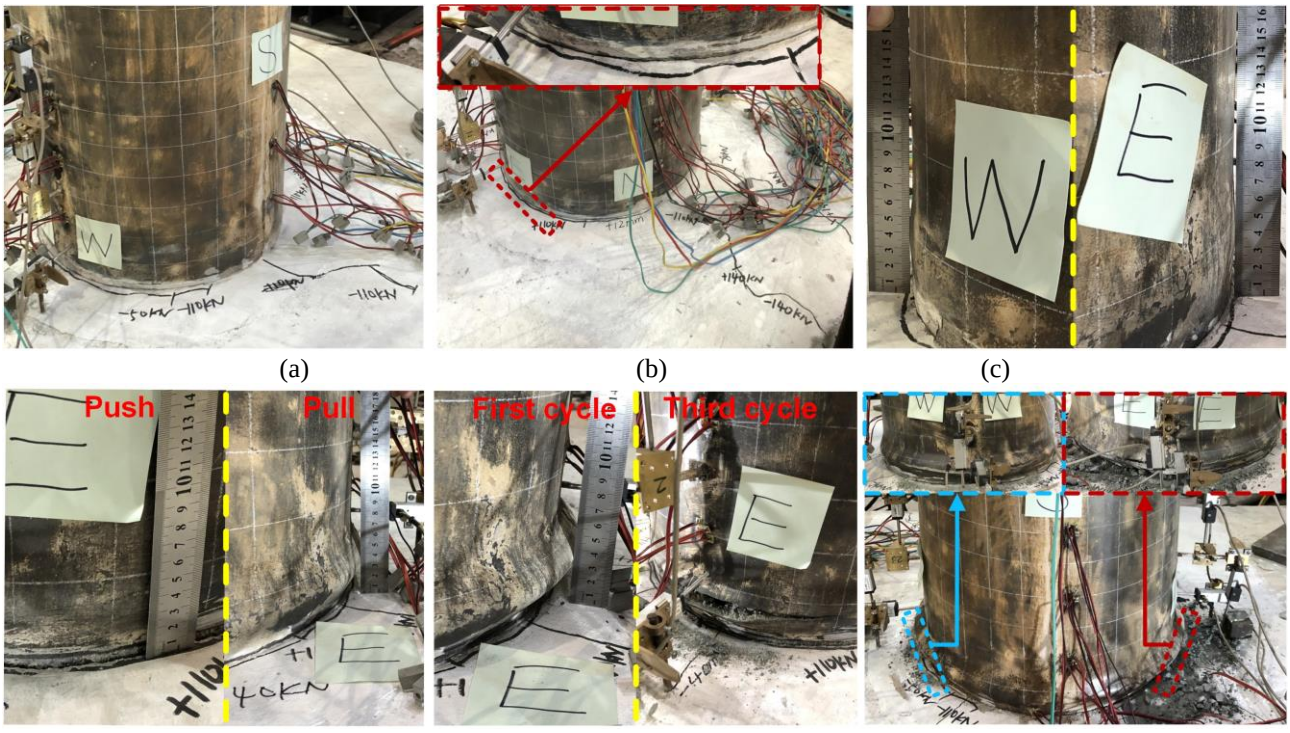

(a) (b) (c)

(d) (e) (f)

Fig. 4. Progression of damage in specimen PCFT-SC: (a) at 0.4% drift, (b) at 0.8% drift, (c) at 1.6% drift, (d) at 3.6% drift, (e) at 5.2% drift, and (f) after the test.

4.2 Force-displacement curves

Fig. 5 shows the cyclic lateral load-drift (displacement) responses of the two PCFT columns and the backbone curve calculated as the average envelope curves considering both the push and pull directions. Fig. 5(a) shows that the PCFT-SC was characterized by a loss of stiffness for drifts larger than 1.6% (triangle symbols). This is due to the yielding of a large region at the bottom side of the steel tube, as observed by the measured tube strain data (discussed in Sect. 4.4), and the tube local buckling illustrated in Fig. 4(c). Nevertheless, tube yielding and buckling did not significantly affect the load-carrying capacity of the PCFT-SC column, which exhibited a steady lateral force until drifts of 5.2%, when the tearing of the steel tube occurred (rhombus symbols in Fig. 5(a)). Fig. 5(a) also highlights the peak forces and the corresponding drifts for both columns and loading directions. The peak forces of PCFT-SC in the push and pull direction were 276.4 and 287.4 kN, respectively, which occurred at drifts of 3.6% and 4.4%, respectively (grey symbols in Fig. 5(a)). By comparing the maximum load capacity of the two PCFT columns, it can be observed that drifts of the peak forces were similar; however, slightly smaller values of the force were observed for the PCFT-SC with respect to the PCFT-HC. Fig. 5(a) shows that the lateral force capacity of PCFT-HC was always slightly higher than that of PCFT-SC. This mainly related to two effects: *1)* the complex state of stress of the steel tube in PCFT-SC, which could deteriorate its bearing capacity and deformation capacity; *2)* the PT force loss measured during the test, which was more significant in the PCFT-SC when compared to the PCFT-HC (discussed in Sect. 4.3). In addition, the intrinsic rocking behavior of PCFT-HC triggered a sizeable amount of elongation in the PT bar, which also contributed to the enhanced lateral resistance of the PCFT column. Upon unloading, the curves of two PCFT columns followed a similar path until the lateral force became zero. After this point, a more notable pinching behavior was observed in the PCFT-SC column, especially after 2.8% drift. This was attributed to the separation between the column and surrounding concrete that occurred at the PCFT-SC column base during loading (Fig. 4(d)). This separation in PCFT-SC would be closing upon the unloading, and the separation in the opposite side of the column was opening on the reverse loading, which led to pinching. A similar phenomenon was also observed in other tests of CFT columns with embedded-based connections [42]. This pinching behavior in PCFT-SC also resulted in its hysteretic loops shape was not plump as that of PCFT-HC. It is noteworthy that

although the PCFT-HC is essentially a rocking system, its self-centering behavior was not clearly visible due to the redundant ED bars (*i.e.*, $\Lambda_c = 2.0 > 1.0$) used in the considered reference specimen.

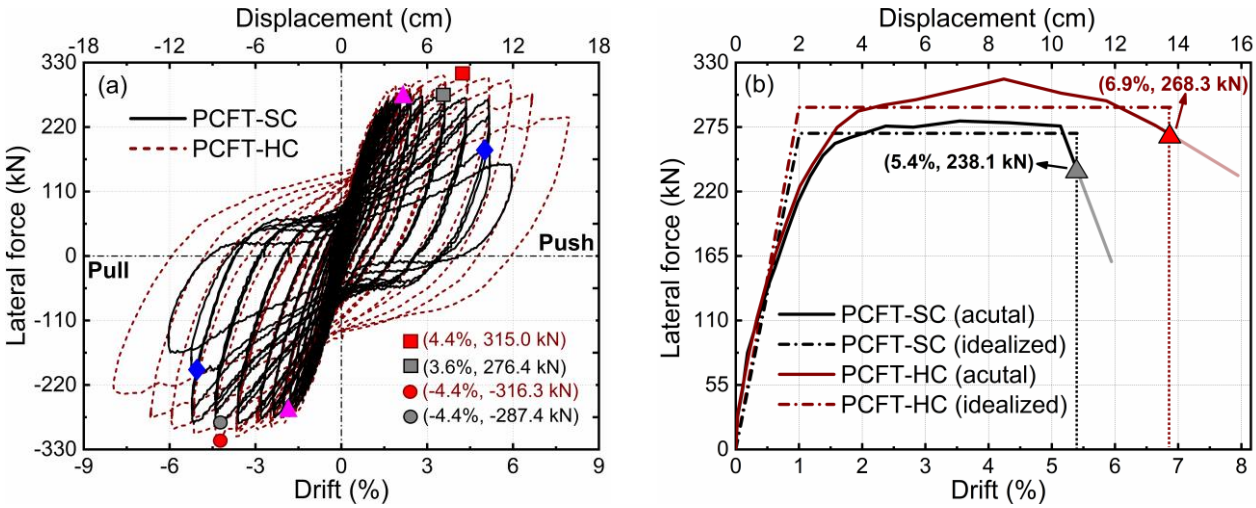

Fig. 5. Lateral force-drift/displacement response: (a) hysteretic curves, (b) average backbone curves.

Fig. 5(b) shows the comparison of average backbone curves considering both the push and pull directions and the corresponding idealized elastoplastic curves highlighting the higher lateral load capacity of the PCFT-HC. Fig. 5(b) also shows that the initial stiffnesses of two PCFT columns were essentially the same. This was expected because the rocking behavior of PCFT-HC was not activated at this stage; thus, the stiffnesses of both PCFT-SC and PCFT-HC were provided by the flexural deformation of CFT columns. Once the interface of PCFT-HC opened (after 0.6% drift [11]), a slightly larger stiffness was observed in PCFT-HC. Based on the idealized bilinear elastoplastic curves determined from the average envelopes [1], the ductility capacity of two PCFT columns was evaluated. The ultimate state was defined corresponding to a degradation in the peak force by 15% and marked with triangle symbols in Fig. 5(b). Table 2 lists the key parameters of the envelope and idealized elastoplastic curves for the two PCFT columns. It can be observed that the yielding of two specimens occurred at the same drift value of 1.0%. The PCFT-HC column experienced a larger ultimate drift of 6.9%, corresponding to a ductility capacity μ_d equal to 6.9. In the PCFT-SC column, the tearing of the steel tube resulted in a sudden drop of the lateral force (Fig. 5(a)), leading to an ultimate drift of 5.4%, corresponding to a ductility capacity μ_d equal to 5.4, which is approximately 21.7% smaller than that of PCFT-HC.

Table 2 Parameters measured of two PCFT columns.

Specimen	Δ_y (%)	F_y (kN)	Δ_p (%)	F_p (kN)	Δ_u (%)	F_u (kN)	μ_d
PCFT-SC	1.0	269.7	3.8	280.1	5.4	238.1	5.4
PCFT-HC	1.0	291.9	4.3	316.0	6.9	268.3	6.9

Note: Δ_y, Δ_p, and Δ_u refer to the equivalent yield, peak, and ultimate drift, respectively; F_y, F_p, and F_u are the equivalent yield, peak, and ultimate force, respectively; μ_d is the drift ductility coefficient, calculated by Δ_u/Δ_y.

4.3 Measured PT stress

Fig. 6 shows the measured stress histories of the PT bars of the two PCFT columns. The initial PT stresses of the two PCFT columns were close (*i.e.*, 268.99 MPa for PCFT-SC; 255.24 MPa for PCFT-HC), with a difference of merely 5.4%. However, this difference gradually increased during the test due to the more considerable PT force loss in the PCFT-SC. After completing the 6.0% drift amplitude, the PT stress values for specimens PCFT-SC and PCFT-HC were respectively equal to 94.54 and 163.21 MPa, corresponding to the stress loss of 174.45 and 92.03 MPa. The higher PT force loss in PCFT-SC is related to the steel tube's local buckling and the consequent column's shortening [43]. Also, the anchorage seating loss in the end anchors of the PT bar during loading could have contributed to the PT force loss. As indicated in Fig. 6(a), the stress of the PT bars in PCFT-SC reached a maximum value of 401.70 MPa at 6.0% drift, which was 20.5% smaller than the corresponding value registered in the PCFT-HC. Additionally, although the stress in the PT bars increased as the applied drift increased, the maximum PT stress values of both PCFT columns throughout the testing were well below the yield stress of the PT bar (*i.e.*, 930 MPa).

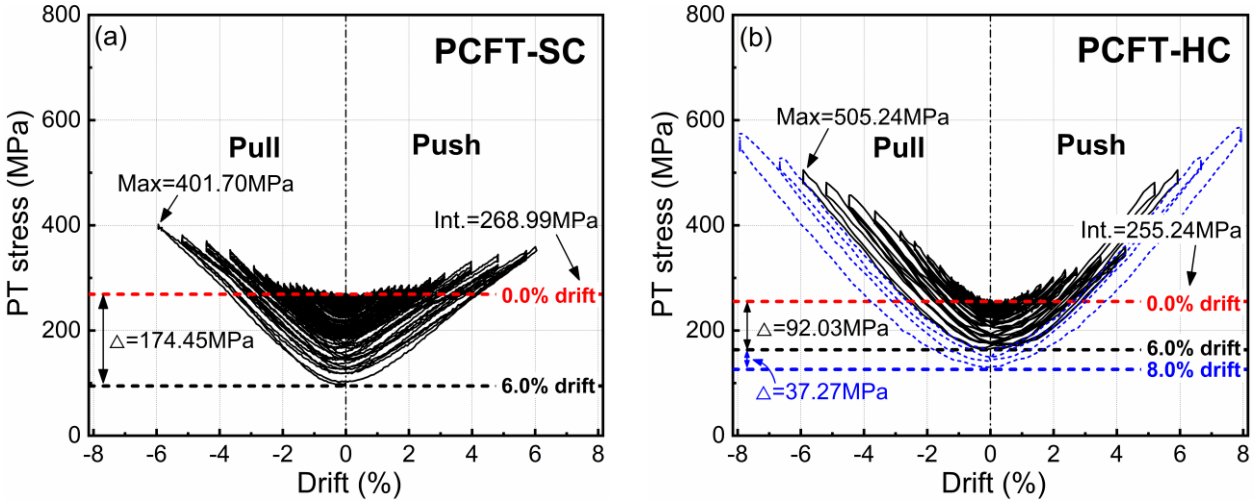

Fig. 6. PT stress versus drift response: (a) PCFT-SC, (b) PCFT-HC.

Fig. 7 shows the PT force loss ratio for PCFT columns at each lateral drift against the corresponding elongation of the PT bar (Δ_{PT}). The PT force loss ratio was computed as the ratio between the resulting PT force loss after completion of each drift level and the initial PT force. Note that the results of the other five PCFT-HC columns specimens tested by Shen *et al.* [11], which were characterized by different design parameters with respect to the *'specimen PCFT-10-3.6'*, are also included in Fig. 7(b) to provide more comprehensive results. It can be observed that for all PCFT columns, the amount of PT force loss increased for increasing Δ_{PT} amplitudes, and linear regressions through the origin provide a good fit of the test results. The slope of each linear regression k and its coefficient of determination R^2 are given in Fig. 7. A larger value of k indicates a more significant PT force loss ratio, while R^2 values close to 1 imply a good fit of the regression line. The results show that linear regression can adequately describe the relationship between the PT force loss and the Δ_{PT} at the applied lateral drifts (all $R^2 > 0.938$). The derived formulations are used in Sect. 5.3 to numerically model the effect of PT force loss.

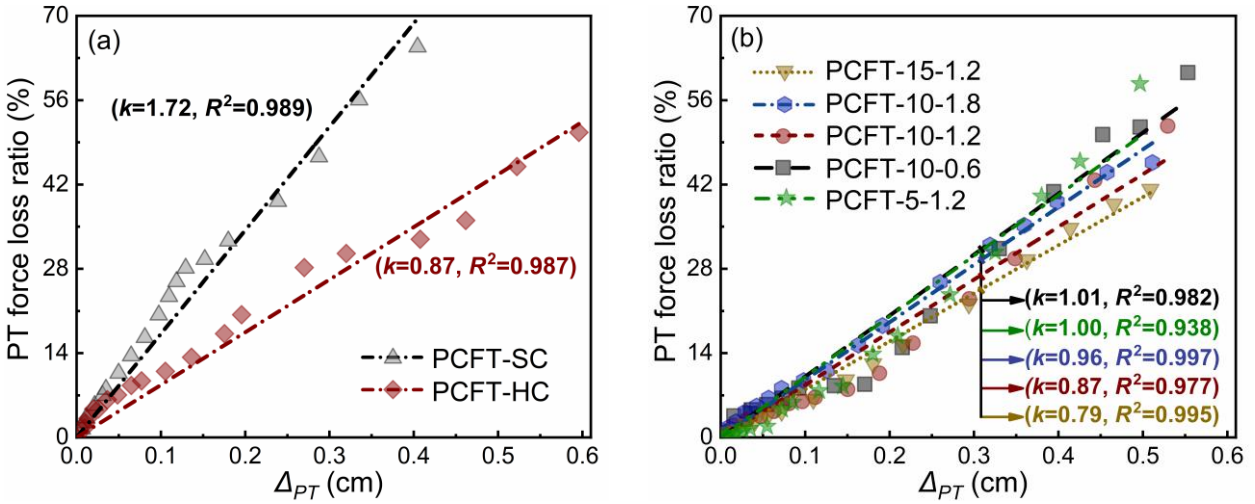

Fig. 7. PT force loss ratio vs. PT bar elongation response: (a) PCFT-SC and PCFT-HC specimens, (b) the other five PCFT specimens with HC details tested in Shen *et al.* [11].

4.4 Column bottom rotation and strain profiles

Based on the damage pattern observed, the bottom region of the PCFT columns was of great concern. Fig. 8 shows the column rotations at four different sections and the steel tube strains at the bottom region for the PCFT-SC and PCFT-HC. The maximum principal strain of the steel tube calculated from the three-directional strain values of strain-gauge rosettes is shown in Fig. 8(b). The rotation values of both columns were calculated based on the LVDT's measurements, and the average rotation along the gauge length of LVDTs was used to represent the experimental rotation (Fig. 8(a)). It is noteworthy that during large drifts (> 4.4% drift), the LVDTs located at the lowermost level of PCFT-HC reached their maximum measuring range and separated from the footing face. Therefore, Fig. 8(a) does not report the rotation data for the PCFT-HC at 5.2% drift. Fig. 8(a) shows that, for both column types, the rotation was nearly concentrated at the base connection (the lowermost height level, 0-15 cm). However, in the PCFT-SC, the rotation spread over a longer length with non-negligible rotation values in the portion 15-27 cm. In reality, the rotation in PCFT-HC at the column base was related to the gap opening at the interface due to the rocking behavior. In this case, the rocking mechanism of the PCFT-

HC relates better to a rigid rotation rather than a flexural deformation, thus resulting in a significant reduction of rotation demand over the height of the column. Conversely, the high concentration of rotation demand in the PCFT-SC is related to the local buckling of the steel tube at the column end, which accommodated most of the deformation of the column during loading.

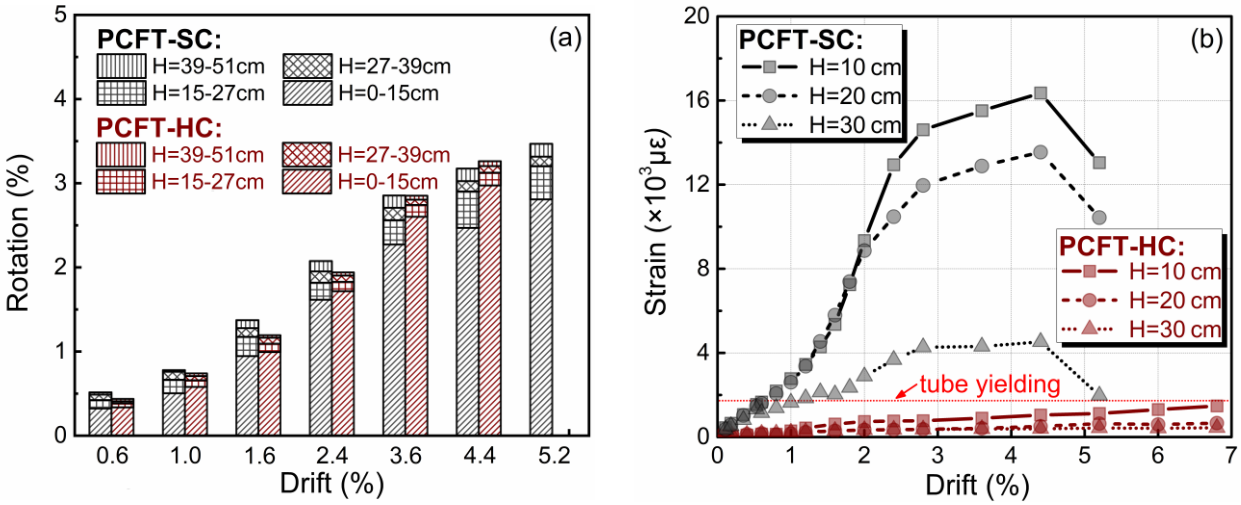

Fig. 8. Comparison of the column bottom response: (a) rotation profiles, (b) the maximum principal strains of steel tube.

Fig. 8(b) shows the maximum principal strain profiles of the steel tube. As expected, the strain values of the steel tube in the PCFT-SC exhibited a significantly higher engagement, and the yielding of the tube (≈ 1800 με, red dotted horizontal line) occurred at a 0.6% drift. Conversely, no yielding was observed in the steel tube of PCFT-HC throughout testing. By comparing the strains in PCFT-SC at three height levels, Fig. 8(b) shows that before 1.6% drift, the strain demands at the heights of 10 cm and 20 cm increased with almost the same trend, both larger than that at 30 cm height. After that (>1.6% drift), a more significant strain increase was observed at the 10 cm height compared with the values obtained at 20 cm height because of the outward buckling of the steel tube near the column end (Fig. 4(c)). At 4.4% drift, the steel tube achieved the maximum strains, with values of 16.4×10^3, 13.5×10^3 and 4.5×10^3 με for 10, 20 and 30 cm height, respectively. The maximum strains at the 10 and 20 cm heights were 3.6 and 3.0 times that measured at the 30 cm height level, which was consistent with the rotation results (Fig. 8(a)), both concentrating at the bottom region less than 20 cm. A drop of strain response was subsequently detected due to the tearing of the steel tube.

4.5 Energy dissipation and residual drifts

A comparison between the two PCFT columns in terms of the ED and self-centering properties is presented in Fig. 9. The equivalent viscous damping ratio ξ_{eq} [19,22] and the normalized residual drift $\widetilde{D}_{rd}$ [23] were employed herein to quantify the ED and self-centering properties respectively computed by Eqs. (5) and (6).

$$\xi_{eq} = \frac{E_d}{4\pi \times E_s} \tag{5}$$

$$D_{rd} = \left| \frac{D_{res}}{D_{imp}} \right| \tag{6}$$

where E_d and E_s are respectively the dissipated energy and stored strain energy in each cycle; and D_{res} and D_{imp} are respectively the residual drift and imposed drift in each cycle. At the lower and moderate lateral drifts (≤ 2.8% drift), both the ξ_{eq} and $\widetilde{D}_{rd}$ did not differ much between the two PCFT columns, implying their ED and self-centering capacities were comparable. The ξ_{eq} and $\widetilde{D}_{rd}$ of the two column types were about 16% and 42% for drift up to 2.8%. However, for both parameters, the difference between the two column types increased for increasing drift amplitudes. The PCFT-SC exhibited lower ξ_{eq} values and higher $\widetilde{D}_{rd}$ response showing a slightly lower seismic performance. This is related to the local buckling of the steel tube, the extensive plastic deformations, and the more significant PT force loss (Figs. 6 and 7(a)). Additionally, the pinching behavior of the PCFT-SC observed in the large drift amplitudes of hysteretic curves (Fig. 5(a)) also impaired the development of its ED capacity as previously presented in Sect. 4.2. However, despite being slightly less performing, the PCFT-SC showed a good seismic behavior that, together with the fabrication advantages, could make it preferable with respect to the PCFT-HC.

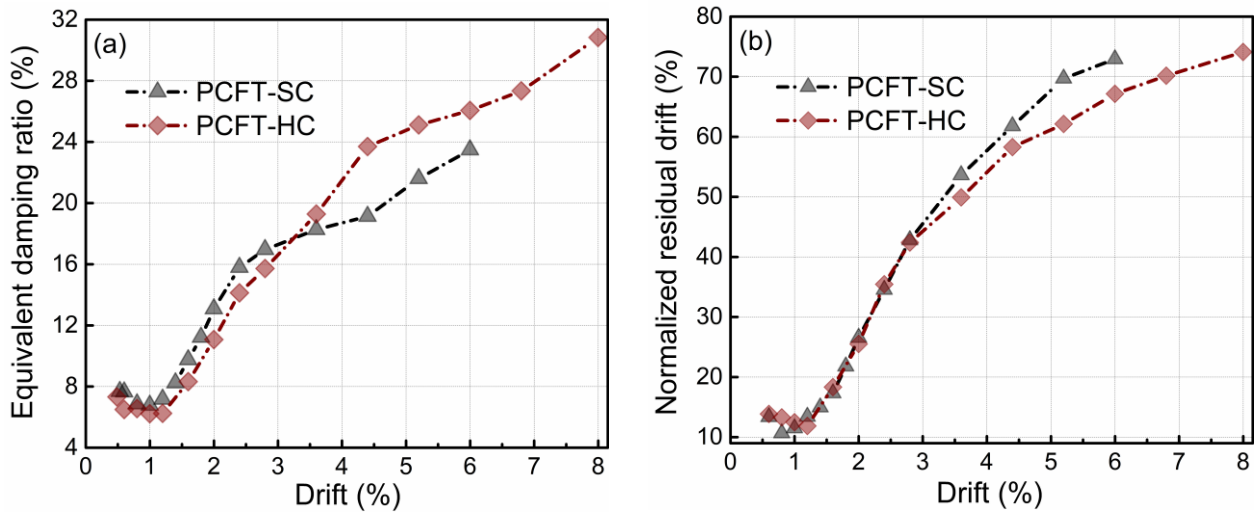

Fig. 9. Energy-dissipation and self-centering capacity: (a) equivalent damping ratio, (b) normalized residual drift.

5. Finite element modeling and validation

Nonlinear FE models were built in OpenSees [44] to simulate the cyclic behavior of PCFT columns with SC and HC base connections. Both the PT force loss and 3D boundary detailing of the base connections were considered in the FE models, and their effectiveness in predicting the cyclic behavior was validated against the experimental results. In addition, the importance of including the effect of PT force loss while simulating the cyclic behavior in PCFT columns was highlighted.

5.1 PCFT-SC modeling

Fig. 10(a) shows the FE model of the PCFT-SC column. The CFT column body was modeled by nonlinear displacement-based beam-column elements with five and fourteen elements in series above and within the footing. The applied vertical constant force was concentrated at the location of the loading point. The elastic flexural stiffness of the CFT column, EI_{CFT}, was defined following the stiffness model proposed by Roeder *et al.* [45]. This model is a variant of the CFT stiffness expressions in AASHTO [1], has been validated by abundant experimental data, and is expressed by the following Eqs. (7) and (8):

$$EI_{CFT} = E_{st}I_{st} + C'E_cI_c \tag{7}$$

$$C' = 0.15 + \frac{P}{P_0} + 2\frac{A_{st}}{A_{st}+A_c} < 0.9 \tag{8}$$

where E_c and E_{st} are respectively the elastic moduli of the concrete core and steel tube; I_c and I_{st} are respectively the moments of inertia of the concrete core and steel tube; and C' is the parameter used to account for the reduction of concrete stiffness, which is related to the axial force ratio, P/P_0, and the areas of the concrete core, A_c, and steel tube, A_{st}, respectively. Fiber discretization was used in the column section (Fig. 10(c)) with the 'Concrete 01' and 'Steel 02' material assigned for the concrete core fill and the steel tube, respectively (Figs. 11(a) and (b)) [27]. The properties of concrete confined by the circular steel tube were defined according to the constitutive law proposed by Han *et al.* [46] according to the following Eqs. (9):

$$y = 2x - x^2 \qquad (x \le 1) \tag{9a}$$

$$y = \begin{cases} 1 + q(x^{0.1\xi} - 1) & (\xi \ge 1.12) \\ \dfrac{x}{\beta(x-1)^2 + x} & (\xi \ge 1.12) \end{cases} \qquad (x > 1) \tag{9b}$$

where $x = \varepsilon/\varepsilon_{cm}$, $y = \sigma/\sigma_{cm}$ with ε_{cm} and σ_{cm} representing the peak strength and the corresponding strain of concrete core, respectively; ξ is the confinement factor [47]; and β is a parameter dependent on ξ and f_c. More details on these parameters are available in the monograph [46]. In the present study, σ_{cm} and ultimate strength, σ_{cu}, for the confined concrete core were equal to 49.3 MPa and 44.2 MPa, with the associated strains ε_{cm} = 0.0036 and ε_{cu} = 0.013. For the steel tube, the yield strength, f_{y_st}, elastic modulus, E_{st}, and post-yield stiffness ratio, b_{st}, were set as 345 MPa, 200 GPa, and 0.01, respectively, according to the manufacturer's data.

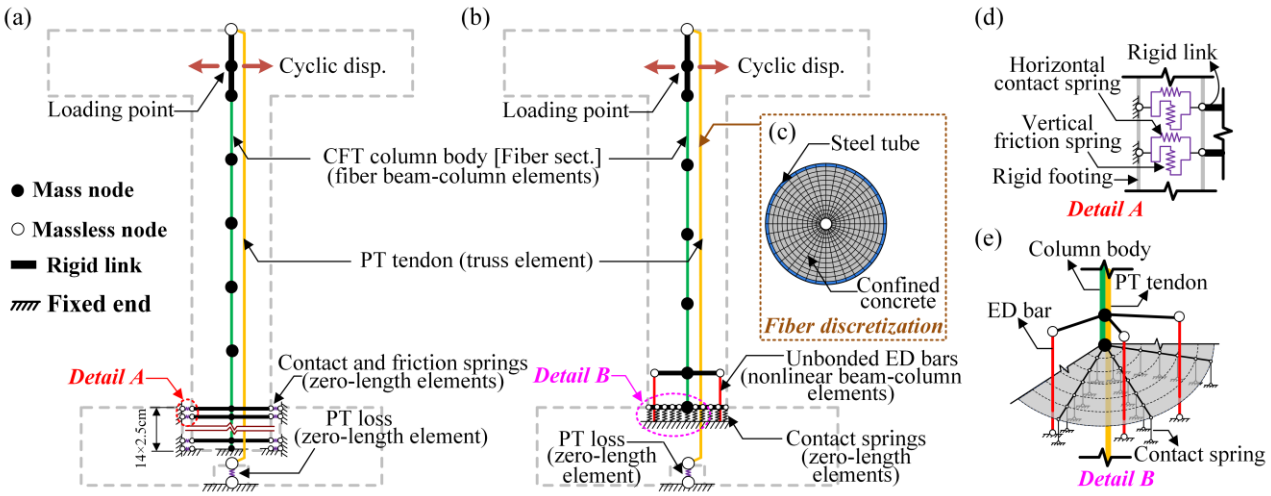

Fig. 10. Numerical model sketches: (a) PCFT-SC column, (b) PCFT-HC column, (c) section fiber discretization, (d) boundary detailing of SC, and (e) boundary detailing of HC.

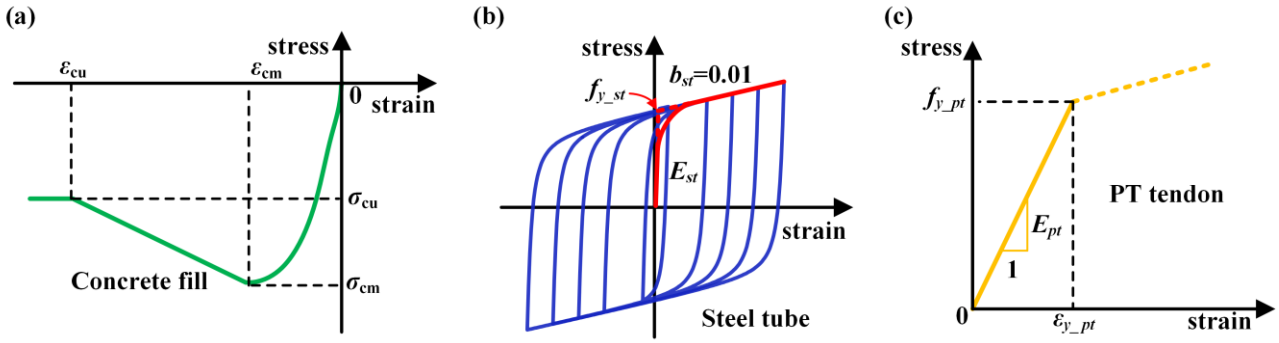

Fig. 11. Material properties of PCFT column shaft: (a) concrete fill, (b) steel tube, and (c) PT bar.

The unbonded PT bar was modeled as an elastic truss element running parallel to the CFT column and connected between the cap beam top and the footing bottom (Fig. 10(a)) [17]. The 'Steel 02' material model with an elastic modulus, E_{PT}, of 195 GPa was used to model the PT bars. The non-linear behavior of the PT bar was modeled with a sharp transition from elastic to the plastic branch (*i.e.*, $cR1$ = 0 [44], Fig. 11(c)) and with a yielding strength, f_{y_pt}, equal to 930 MPa. However, yielding of the PT bar was not expected in the numerical simulations. To account for the PT force loss during the cyclic analysis, a zero-length element was introduced between the PT bar bottom and the fixed anchor end [13] (see Fig. 10(a)). The definition of the zero-length element properties, based on the test results, are discussed in Sect. 5.3.

Multiple zero-length elements were used to simulate the boundary conditions within the embedment length (Fig. 10(a)). The interface between the column and the footing within the embedment length was discretized into 14 levels along with the height, and 36 segments along the circumference, resulting in a 3D SC connection boundary with a total of 504 zero-length elements. These elements were rigidly connected to the column body. Each element included a horizontal contact spring and a vertical friction spring working in parallel (*Detail A*, Fig. 10(d)) defined respectively by the 'Elastic-no tension' material (Fig. 12(a)) and the 'Elastic uniaxial' material (Fig. 12(b)) in OpenSees [38]. The compression stiffness of the horizontal contact spring, k_{hc}, affects the initial stiffness of the PCFT-SC column, k_{PCFT_SC}, which can be approximately obtained by the following Eq. (10):

$$\frac{1}{k_{PCFT\_SC}} = \frac{1}{k_{CFT}} + \frac{1}{2k_{hc}} \tag{10}$$

where k_{CFT} is the stiffness provided by the CFT column body. k_{CFT} can be calculated by the following Eq. (11):

$$k_{CFT} = 3 \times EI_{CFT} / H_{CFT} \tag{11}$$

where H_{CFT} is the clear height of the CFT column. According to this equation, the stiffness provided by the CFT column body k_{CFT} is equal to 3.41 × 10^4 N/mm. Moreover, the initial stiffness of the PCFT-SC column, k_{PCFT_SC}, was assumed equal to 2.84 × 10^4 N/mm based on the experimental data. By inverting Eq. (10), the stiffness k_{hc} was calculated to be 9.0 × 10^4 N/mm. The stiffness of the vertical friction spring, k_{vf}, was chosen to be 0.3k_{hc} considering conventional values for friction coefficient between the sliding surfaces of steel and concrete [48]. Fig. 12(c) shows the results of a preliminary numerical simulation of a push and pull cyclic load with small drifts (≈ 0.12% drift). The comparison of the hysteretic curves between the simulation and experimental results shows an overall good agreement in terms of the stiffness between

the experimental test and the numerical analysis, indicating the selected stiffness values for the SC detailing model were appropriate.

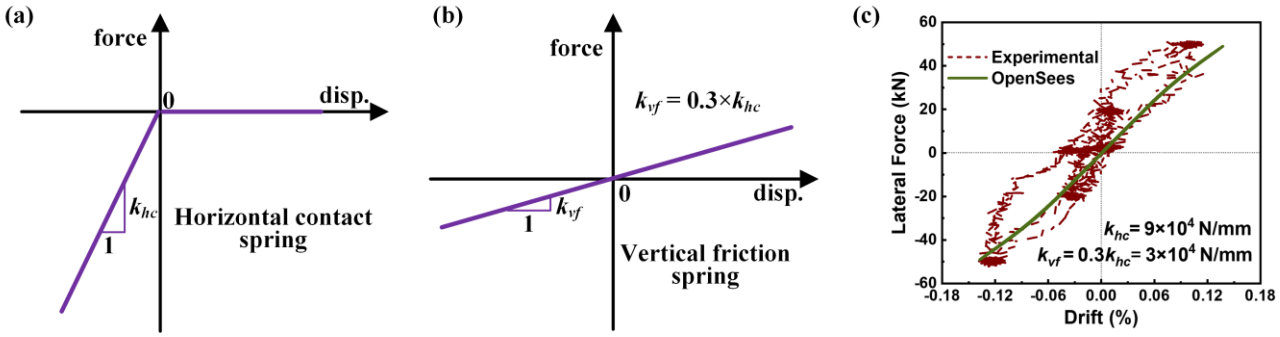

Fig. 12. Analysis model of the boundary of SC: (a) horizontal contact, (b) vertical friction, and (c) comparison of hysteretic curves under the selected spring stiffnesses (≈ 0.12% drift).

5.2 PCFT-HC modeling

Fig. 10(b) shows the FE model of the PCFT-HC column. The elements and material models of the CFT column, cap beam, and PT bar for PCFT-HC were identical to those used in the FE model of PCFT-SC (previously described). The model of the HC base connection was characterized by the details of the ED bars and the rocking phenomenon, which required careful modeling. All ED bars were represented by nonlinear beam-column elements and evenly distributed around the column circumference (*Detail B*, Fig. 10(e)). The upper ends of ED bars were connected to the intermediate nodes of the column by rigid links, while the lower ends were fully fixed. Note that the strain penetration of ED bars was considered in the FE model by introducing an additional equivalent unbonded length, L_{eu}, at the two ends of ED bars [12,18,30]. The value of L_{eu} was taken to be equal to 5.5 times the bar diameter according to test strain data of ED bar in the PCFT-HC column performed by the authors. A trilinear 'Hysteretic' material model was adopted to simulate the nonlinear characteristics of the ED bars (Fig. 13(a)). Three turning points in the 'Hysteretic' material envelope were defined as the yield state (ε_{y_ED} = 0.24%, f_{y_ED} = 506.2 MPa), peak state (ε_{p_ED} = 0.08, f_{p_ED} = 692.3 MPa), and ultimate state (ε_{u_ED} = 0.15, f_{u_ED} = 468.4 MPa), respectively, which were set according to coupon tests. The optimization method proposed by Stephens *et al.* [27] was used to determine the damage parameters of the 'Hysteretic' material model corresponding to *damage1* = 0.05, *damage2* = 0.58, *pinchX* = 0.05, and *pinchX* = 0.90, while no degraded unloading stiffness was introduced [44].

Several zero-length elements were introduced at the column base to simulate the rocking interface (Fig. 10(b)) [10]. These multi-spring elements formed a 3D interface boundary, discretized into 5 rings along the radius and 36 wedges along the circumference (Fig. 10(e)). The 'Concrete 01' nonlinear material model, characterized by a compression-only behavior, was applied to these elements to simulate the gap opening phenomenon [29]. The compressive behavior of the UHPC mortar bed was used to simulate the contact springs. By considering the discretization of the rocking interface, the force-displacement relationship can be derived from the stress-strain relationship of the mortar bed and assigned to each contact spring, as shown in Fig. 13(b). Stresses in the stress-strain relationship should be multiplied by the spring influence area, A_{infl}, and the strains should be amplified by the theoretical neutral axial depth (d_{theo}) following the recommendations of Li *et al.* [10] and Guerrini *et al.* [29]. The d_{theo} was set equal to 0.25 times the column diameter herein. Peak stress, σ_m = 122 MPa and peak strain, ε_m = 0.37% for UHPC mortar bed were obtained from coupon tests [11], and its ultimate capacity (ε_u = 0.78%, σ_u = 36.6 MPa) was determined based on the formulation of Wang *et al.* [49].

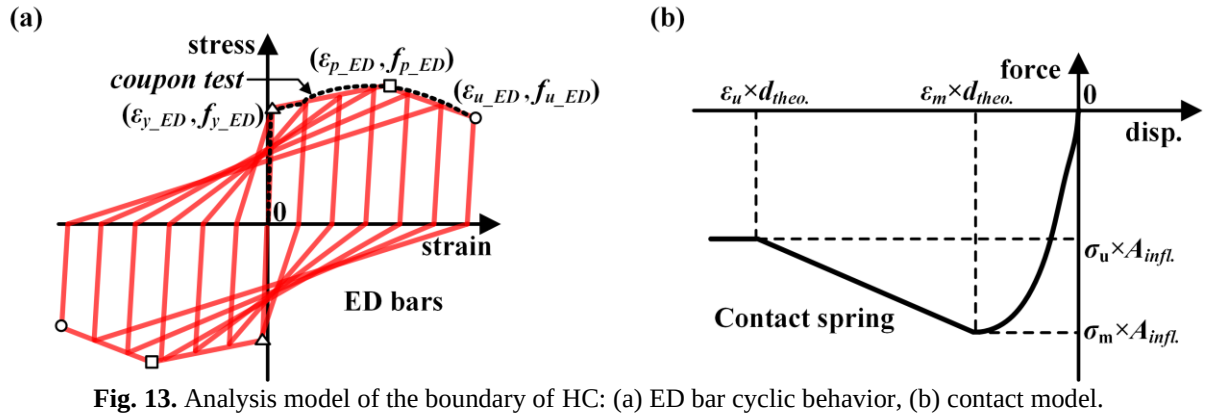

Fig. 13. Analysis model of the boundary of HC: (a) ED bar cyclic behavior, (b) contact model.

5.3 PT force loss modeling

At the applied i^{th} peak drift, the maximum PT force (P_{max_i}) considering the PT force loss during i^{th} drift loading (P_{loss_i}) can be expressed by the following Eq. (12):

$$P_{max\_i} = P_{res\_i-1} + k_{PT} \times \Delta_{PT\_i} - P_{loss\_i} \tag{12}$$

or alternatively by the following Eqs. (13):

$$P_{max\_i} = P_{res\_i-1} + \alpha k_{PT} \times \Delta_{PT\_i} \qquad \alpha = 1 - \frac{P_{loss\_i}}{\Delta_{PT\_i}} \times \frac{1}{k_{PT}} \tag{13}$$

where $P_{res\_i\text{-}1}$ is the residual PT force after completion of the i-1^{th} drift, *i.e.*, the maximum PT force experienced before applying the i^{th} drift; k_{PT} is the axial stiffness of the PT bar; Δ_{PT_i} is the elongation of the PT bar during the i^{th} drift loading; and α is a factor reflecting the influence of PT force loss. Thus, the effect of the PT force loss on load resistance can be considered by the product of the k_{PT} with the factor α. According to this formulation, and to implement the PT force loss in the FE models, a zero-length element, with rigid plastic behavior, was placed in series with the PT tendon, as shown in Figs. 10(a), 10(b) and 14 (a). The rigid plastic behavior was simulated by the 'Multilinear' material model characterized by a large initial stiffness (*i.e.*, 1000 k_{PT}) and by a yielding strength equal to the initial PT force (F_{PT0}). The strain hardening can be calibrated against the experimental results for each i^{th} drift to simulate the PT force loss. This calibration can be easily obtained by considering a strain hardening given by the product n_i k_{PT} for each Δ_{PT_i} where Δ_{PT_i} represents the elongation of PT bar at the i-1^{th} drift. The resulting PT bar stiffness at the Δ_{PT_i} (k'_{PT_i}) can be calculated by the following Eqs. (14):

$$k'_{PT\_i} = \frac{1}{1/k_{PT} + 1/n_i k_{PT}} = \frac{n_i}{n_i + 1} k_{PT} \tag{14}$$

where the n_i parameter is defined such that k'_{PT_i} is equivalent to the αk_{PT} in Eqs. (13) and can be calculated as follow:

$$n_i = \frac{P_{loss\_i}}{\Delta_{PT\_i}} \times \frac{1}{k_{PT}} - 1 \tag{15}$$

For the considered PCFT columns, the relationships between the PT force loss and PT bar elongation obtained experimentally in Sect. 4.3, and illustrated in Fig. 7, show that the ratio P_{loss_i}/Δ_{PT_i} is constant. This leads to a constant parameter n_i (see Fig. 14(b)) corresponding to 0.61 and 2.28 for PCFT-SC and PCFT-HC, respectively.

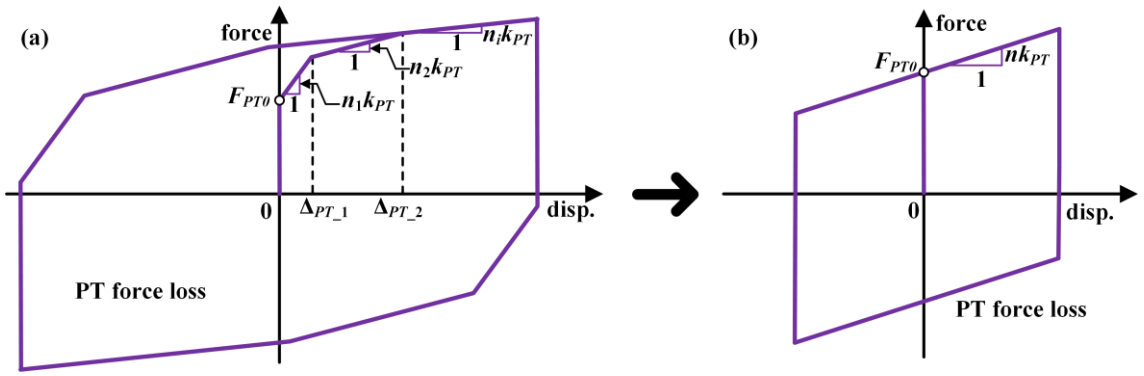

Fig. 14. Analysis model of the loss of PT force: (a) theoretical PT force loss model, (b) adopted PT force loss model.

5.4 Finite Element (FE) model validation

The OpenSees models were validated against the experimental results of the quasi-static tests. Fig. 15 shows the comparison of experimental and numerical results for the PCFT-SC specimen in terms of lateral force-drift cyclic curves (Fig. 15(a)) and PT force history response (Fig. 15(b)). The comparison is performed up to a drift equal to 5.2% where the steel tube fractured in the experimental tests. The responses of the simulations without considering the PT force loss effects are also plotted in the Figures. Note that for a clearer comparison, the backbone rather than the cyclic curve of the case without PT force loss is shown in Fig. 15(a), while the backbone curves of the PT force histories are plotted in Fig. 15(b). In general, a good agreement was achieved between the test data and OpenSees numerical results for PCFT-SC. However, a small difference between experimental and numerical force in the pull direction was observed (Fig. 15(a)). This is due to the material inhomogeneity and construction tolerances, which resulted in a small asymmetry of the experimental response of the column. In addition, it was observed that neglecting the PT force loss effects would exaggerate the force resistance of the column, especially for large drifts. As shown in Fig. 15(a), for a drift of 5.2%, the simulation case that neglects the PT force loss overestimated the force resistance by 6.2% compared to the simulation case with PT force loss. Fig. 15(b) compares the variation of the numerical and experimental PT force histories with the

increasing loading steps. The results show the importance of accounting for this effect and, at the same time, that the proposed modeling strategy is adequate in simulating the progressive PT force loss observed in the experimental test. When the PT force loss effect is excluded from the analysis, significant differences can be observed in comparison with test results.

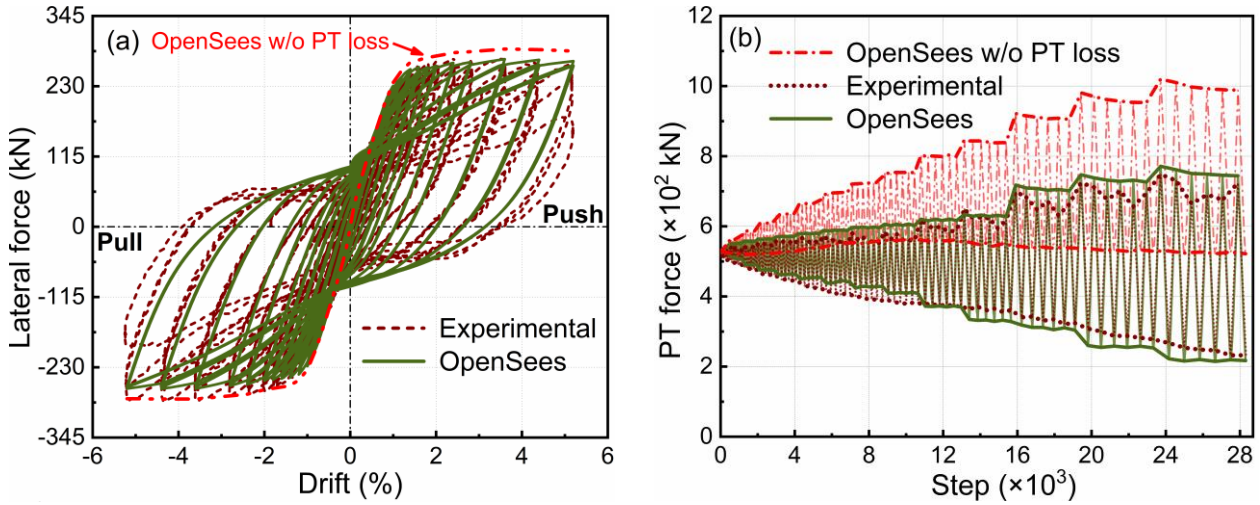

Fig. 15. Comparison of the numerical and experimental responses for PCFT-SC: (a) cyclic load-drift behavior, (b) PT force history.

A similar comparison was also presented for the responses of the PCFT-HC column, as shown in Fig. 16. Also in this case, the results show a good agreement between the test data and OpenSees numerical results both in terms of lateral force-drift cyclic curves (Fig. 16(a)) and PT force histories (Fig. 16(b)). The good correlation between the simulation and test results showed the adequacy of the FE model in evaluating the cyclic behavior of the PCFT-HC column. When the PT force loss was not included in the FE model, the similar phenomenon of overestimating force resistance and PT force as that in the PCFT-SC was observed in PCFT-HC, which led to the increase of the errors in predicting seismic performance for the FE model of PCFT-HC. At 5.2% drift, the lateral force calculated by the model without the inclusion of PT loss was 5.6% greater than that obtained from the FE model with the inclusion of PT loss; however, this error percentage increased to 18.9% at the 6.8% drift. Furthermore, it is worth highlighting that the amount of PT loss in the simulation of the PCFT-HC is less than that in the PCFT-SC case because a larger *n* value was used in FE model of PCFT-HC. Fig. 17 provides the comparison results on the other five PCFT columns with HC tested by Shen *et al.* [11], which again confirmed the effectiveness of the developed PCFT-HC FE model considering PT force loss.

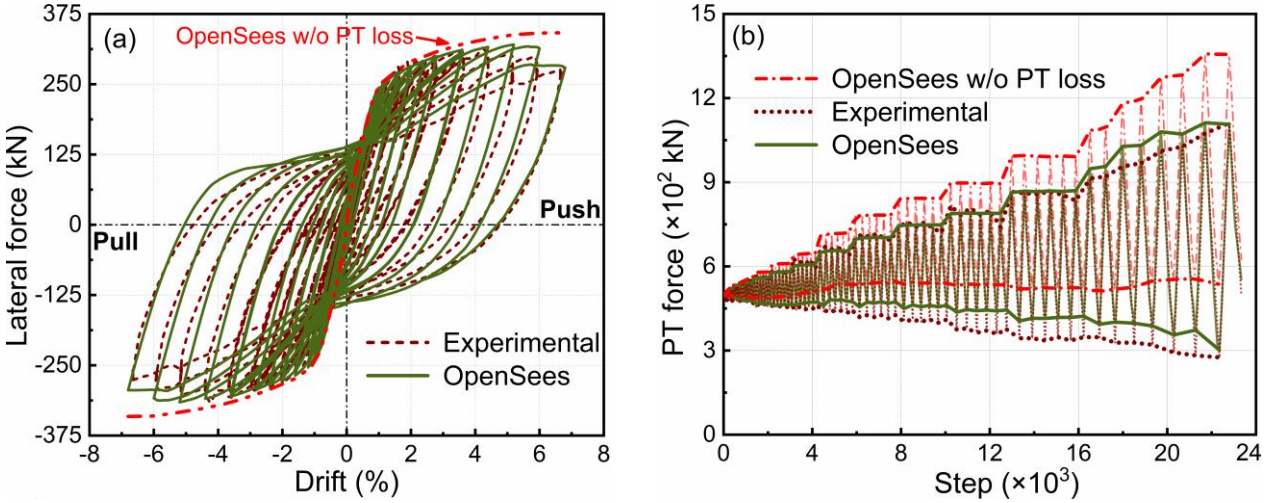

Fig. 16. Comparison of the numerical and experimental responses for PCFT-HC: (a) cyclic load-drift behavior, (b) PT force history.

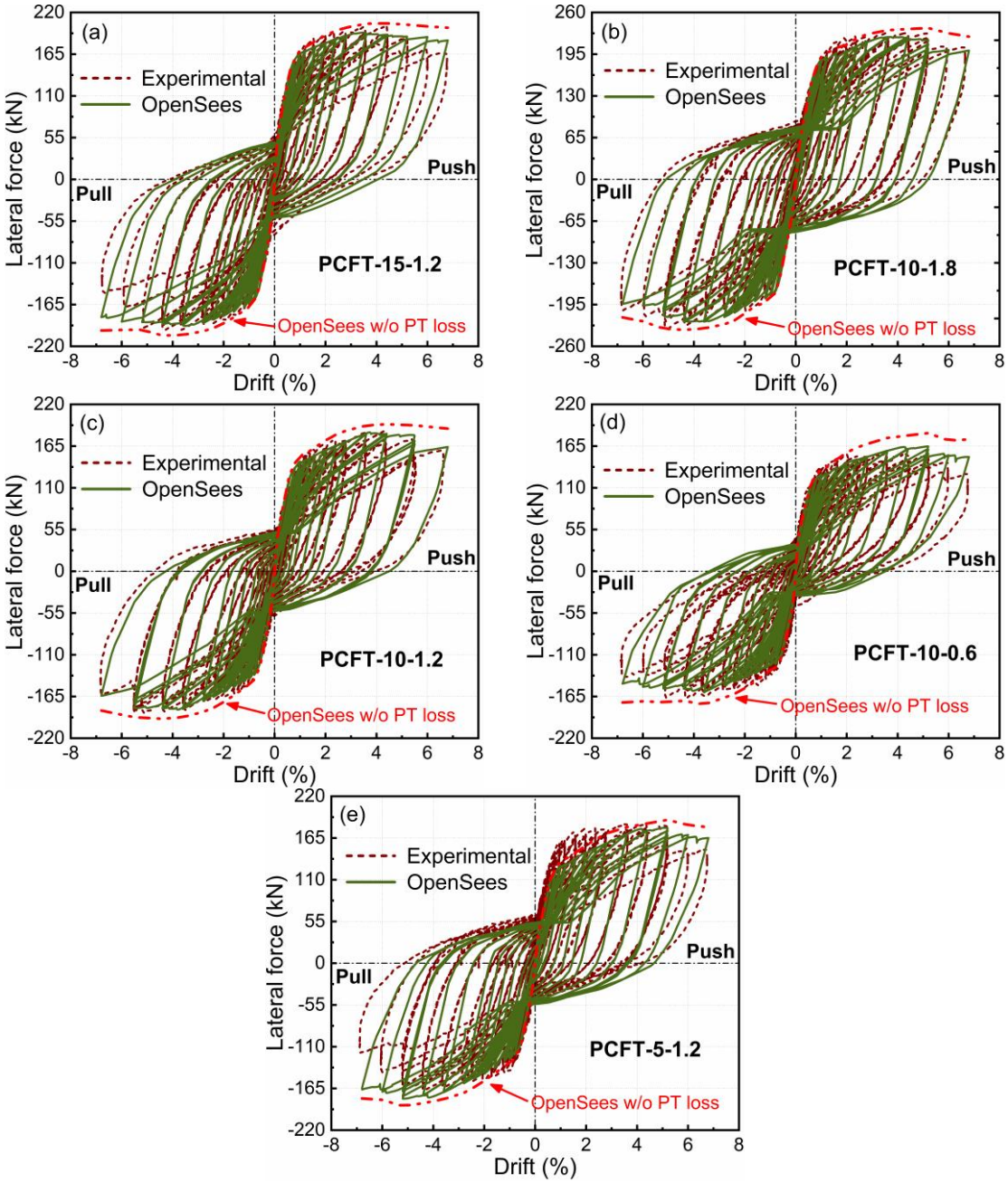

Fig. 17. Comparison between numerical and experimental hysteretic results for the other five PCFT specimens with HC details tested by Shen *et al.* [11]: (a) PCFT-15-1.2, (b) PCFT-10-1.8, (c) PCFT-10-1.2, (d) PCFT-10-0.6, and (e) PCFT-5-1.2.

6. Conclusions

The present paper experimentally and numerically investigates an innovative column-footing socket connection (SC) for post-tensioned concrete-filled steel tube (PCFT) columns (*i.e.*, PCFT-SC column). The embedded steel tube contributes to the lateral resistance of the column and dissipates the seismic input energy while the post-tensioned (PT) bars are used to improve its self-centering behavior. The use of steel tubes to encase the column is a relatively simple and practical solution with multiple benefits: from one hand, it increases the confinement of the concrete; on the other hand, the steel tube act as formwork for casting, thus promoting the Accelerated Bridge Construction (ABC) objectives.

The seismic behavior of PCFT-SC was investigated through a quasi-static experimental test providing information in terms of applied drifts versus lateral force, post-tensioned (PT) force in the PT bar, column rotations, tube strain profiles, energy dissipation (ED), and residual drift relationships. The experimental results are compared with those of a PCFT column with a hybrid connection (PCFT-HC) previously investigated by the authors. Based on the test observations, finite element (FE) models of these two PCFT column types incorporating the effects of PT force loss and detailed column base connections modeling were developed and validated in OpenSees. The quasi-static experimental test and the numerical analyses led to the following conclusions:

(1) The emulative SC represents an effective and viable solution in PCFT column and demonstrated its ability to achieve large drifts (ultimate drift of 5.4%) without experiencing a sudden degradation of lateral load resistance. Both load and ductility capacity are close to (slightly lower) the previously investigated PCFT-HC column.

(2) After completion of the test, the SC exhibited no damage, except for some minor cracks at the footing. Most damages occurred at the bottom region of the column body (within a height of 5 cm) and included the local buckling and eventual fracture of the steel tube and the crushing of the concrete core.

(3) The use of PT bars in the PCFT-SC to some extent increased its self-centering capability while the embedment of the steel tube within the footing provided sufficient energy dissipation for PCFT-SC. For drifts lower than 2.8%, its self-centering and ED capacities were comparable to those of the PCFT-HC column. For larger drifts, the development of the tube local buckling and the significant PT force loss impaired the self-centering and ED capabilities of the PCFT-SC which showed a reduced seismic performance with respect to the PCFT-HC.

(4) Significant PT force loss was observed in PFCT-SC, especially during large drift cycles. This can be related to column shortening caused by the local buckling of the steel tube and the potential anchorage seating loss of PT tendons. It has been observed that a linear regression model passing through the origin represents an appropriate model able to describe the relationship between the PT force loss and the PT bar elongation for both PCFT-SC and PCFT-HC columns. Thus, more attention should be paid to the anchorage issues of the PT bar for the convenience of re-tensioning or limiting anchorage seating loss after severe earthquakes.

(5) The FE models of the PCFT-SC and PCFT-HC columns with the detailed boundary conditions can capture their respective experimental cyclic responses when the linear PT force loss model is considered. Disregarding the effect of PT force loss in numerical analyses leads to an overestimation of the load capacity of both PCFT column types, especially for large drifts.

(6) Overall, the PCFT-SC demonstrated to be an appropriate option for bridge columns in both moderate and high seismic regions. However, further studies are necessary to define tailored details able to control the PT force loss and limit the tube buckling, which could significantly affect the self-centering capacity of the column. Possible solutions could include the use of stiffening ribs or shear studs on the tube inner surface. Moreover, additional studies are required to evaluate the impact of the salient parameters such as the properties of the annular ring and embedded length, the tube geometry, and the initial PT force on the seismic response of the PCFT-SC.

Acknowledgments

The financial support provided by the National Natural Science Foundation of China (Grant No.51838010) is greatly appreciated by the authors. The first author also gratefully acknowledges the China Scholarship Council (Grant No.202006260245) for financial support of visiting at UCL.

References

[1] AASHTO. AASHTO guide specifications for LRFD seismic bridge design. Washington (DC): American Association of State Highway Transport Officials; 2015.

[2] MOHURD. Code for seismic design of urban bridge (CJJ 166-2011). Beijing: China Architecture and Building Press; 2011. (in Chinese)

[3] EN 1998-1. Eurocode 8: Design of structures for earthquake resistance − Part 1: General rules, seismic actions, and rules for buildings. Brussels: European Committee for Standardization; 2004.

[4] ANSI/AISC 341-16. Seismic provisions for structural steel buildings. Chicago: American Institute of Steel Construction; 2016.

[5] ASCE/SEI 7-16. Minimum design loads and associated criteria for buildings and other structures. Reston: American Society of Civil Engineers; 2017.

[6] JRA. Design specifications of highway bridges − Part 5: seismic design. Tokyo: Japan Road Association; 2016.

[7] Freddi F, Galasso C, Cremen G, Dall'Asta A, Sarno, LD, Giaralis A et al. Wardman J, Woo G. Innovations in earthquake risk reduction for resilience: recent advances and challenges. Int J Disaster Risk Reduct. 2020; 60: 102267.

[8] Mortagi M, Ghosh J. Concurrent modelling of carbonation and chloride-induced deterioration and uncertainty treatment in aging bridge fragility assessment. Struct Infrastruct Eng. 2020; DOI: 10.1080/15732479.2020.1838560.

[9] SMarsh ML, Wernli M, Garrett BE, Stanton JF, Eberhard MO, Weinert MD. Application of accelerated bridge construction connections in moderate-to-high seismic regions. NCHRP Research Report 698. Washington (DC): The National Academics Press; 2011.

[10] Li Y, Li J, Shen Y. Quasi-static and nonlinear time-history analyses of post-tensioned bridge rocking piers with internal ED bars. Structures. 2021; 32: 1455-68.

[11] Shen Y, Liu X, Li Y, Li J. Cyclic tests of precast post-tensioned concrete filled steel tubular (PCFT) columns with internal energy-dissipating bars. Eng Struct. 2021; 229: 111651.

[12] Bu Z, Ou Y, Song J, Zhang N, Lee GG. Cyclic loading test of unbonded and bonded posttensioned precast segmental bridge columns with circular section. J Bridge Eng. 2016; 21(2): 04015043.

[13] Freddi F, Dimopoulos C, Karavasilis TL. Rocking damage-free steel column base with friction devices: design procedure and numerical evaluation. Earthq Eng Struct Dyn. 2017; 46(14): 2281-300.
[14] Freddi F, Dimopoulos C, Karavasilis TL. Experimental evaluation of a rocking damage-free steel column base with friction devices. J Struct Eng. 2020; 146(10): 04020217.
[15] Elettore E, Freddi F, Latour M, Rizzano G. Design and analysis of a seismic resilient steel moment resisting frame equipped with damage-free self-centering column bases. J Constr Steel Res. 2021; 179: 106543.
[16] Marriott D, Pampanin S, Palermo A. Quasi-static and pseudo-dynamic testing of unbonded post-tensioned rocking bridge piers with external replaceable dissipaters. Earthq Eng Struct Dyn. 2009; 38: 331-54.
[17] Jeong HI, Sakai J, Mahin SA. Shaking table tests and numerical investigation of self-centering reinforced concrete bridge columns. PEER Report 2008/06. Berkeley, USA: Pacific Earthquake Engineering Research Center, University of California; 2008.
[18] Ou Y, Wang P, Tsai M, Chang K, Lee GG. Large-scale experimental study of precast segmental unbonded posttensioned concrete bridge columns for seismic regions. J Struct Eng. 2010; 136(3): 255-64.
[19] Hassanli R, Youssf O, Mills JE. Seismic performance of precast post-tensioned segmental FRP-confined and unconfined crumb rubber concrete. J Compos Constr. 2017; 21(4): 04017006.
[20] Li C, Bi K, Hao H. Seismic performances of precast segmental column under bidirectional earthquake motions: Shake table test and numerical evaluation. Eng Struct. 2019; 187: 314-28.
[21] Trono W, Jen G, Panagiotou M, Schoettler M, Ostertag CP. Seismic response of a damage-resistant recentering posttensioned-HYFRC bridge column. J Bridge Eng. 2015; 20(7): 04014096.
[22] Wang Z, Wang J, Tang Y, Liu T, Gao Y, Zhang J. Seismic behavior of precast segmental UHPC bridge columns with replaceable external cover plates and internal dissipaters. Eng Struct. 2018; 177: 540-55.
[23] Moustafa, A, ElGawady MA. Shaking table testing of segmental hollow-core FRP-concrete-steel bridge columns. J Bridge Eng. 2018; 23(5): 04018020.
[24] Chou C, Chang H, Hewes JT. Two-plastic-hinge and two dimensional finite element models for post-tensioned precast concrete segmental bridge columns. Eng Struct. 2013; 46: 205-17.
[25] Guerrini G, Restrepo JI, Massari M, Vervelidis A. Seismic behavior of posttensioned self-centering precast concrete dual-shell steel columns. J Struct Eng. 2015; 141(4): 04014115.
[26] Wang X, Xie C, Lin L, Li J. Seismic behavior of self-centering concrete-filled square steel tubular (CFST) column base. J Constr Steel Res. 2019; 156: 75-5.
[27] Stephens MT, Lehman DE, Roeder CW. Seismic performance modeling of concrete-filled steel tube bridges: tools and case study. Eng Struct. 2018; 165: 88-105.
[28] Chou C, Chen Y. Cyclic tests of post-tensioned precast CFT segmental bridge columns with unbonded strands. Earthq Eng Struct Dyn. 2006; 35: 159-75.
[29] Guerrini G, Restrepo JI, Vervelidis A, Massari M. Self-centering precast concrete dual-steel-shell columns for accelerated bridge construction: seismic performance, analysis, and design. PEER Report 2015/13. Berkeley, USA: Pacific Earthquake Engineering Research Center, University of California; 2015.
[30] Tobolski MJ. Improving the design and performance of concrete bridges in seismic regions. PhD Thesis. San Diego: University of California; 2010.
[31] Stephens MT, Lehman, DE, Roeder CW. Design of CFST column-to-foundation/cap beam connections for moderate and high seismic regions. Eng Struct. 2016; 122: 323-37.
[32] Stephens MT, Berg LM, Lehman DE, Roeder CW. Seismic CFST column-to-precast cap beam connections for accelerated bridge construction. J Struct Eng. 2016; 142(9): 04016049.
[33] Lehman DE, Roeder CW. Foundation connections for circular concrete-filled tubes. J Constr Steel Res. 2012; 78: 212-25.
[34] White S, Palermo A. Quasi-static testing of posttensioned nonemulative column-footing connections for bridge piers. J Bridge Eng. 2016; 21(6): 04016025.
[35] Haraldsson OS, Janes TM, Eberhard MO, Stanton JF. Seismic resistance of socket connection between footing and precast column. J Bridge Eng. 2013; 18(9): 910-19.
[36] Khaleghi B, Schultz E, Seguirant S, Marsh L, Haraldsson O, Eberhard M et al. Accelerated bridge construction in Washington State: from research to practice. PCI J. 2012; 57(4): 34-49.
[37] Wang Z, Li T, Qu H, Wei H, Li Y. Seismic performance of precast bridge columns with socket and pocket connections based on quasi-static cyclic tests: experimental and numerical study. J Bridge Eng. 2019; 24(11): 04019105.
[38] Xu Y, Zeng Z, Wang Z, Ge J. Experimental studies of embedment length of precast bridge pier with socket connection to pile cap. Eng Struct. 2021; 233: 111906.
[39] MOHURD. Technical code for concrete filled steel tubular structures (GB 50936-2014). Beijing: China Architecture and Building Press; 2014. (in Chinese)
[40] Wang J, Sun Q, Li J. Experimental study on seismic behavior of high-strength circular concrete filled thin-walled steel tubular columns. Eng Struct. 2019; 182: 403-15.
[41] Xu S, Wu C, Liu Z, Shao R. Experimental investigation on the cyclic behaviors of ultra-high performance steel fiber reinforced concrete filled thin-walled steel tubular columns. Thin-Walled Struct. 2019; 140: 1-20.
[42] Rehmat S, Sadeghnejad A, Mantawy IM, Azizinamini A. Experimental study on concrete filled steel tubes to footing

connection using ultra-high performance concrete. Eng Struct. 2021; 242: 112540.
[43] Garlock MM, Ricles JM, Sause R. Experimental studies of full-scale posttensioned steel connections. J Struct Eng. 2015; 131(3): 438-48.
[44] Mazzoni S, McKenna F, Scott MH, Fenves GL. OpenSees: Open System for earthquake engineering simulation. Pacific Earthquake Engineering Research Centre (PEER), University of California, Berkley, California, 2009. Available at http://opensees.berkeley.edu.
[45] Roeder CW, Lehman DE, Bishop E. Strength and stiffness of circular concrete-filled tubes. J Struct Eng. 2016; 136(12): 1545-53.
[46] Han L. Concrete filled steel tublar structures-theory and practice. 3rd edition. Beijing: Science Press; 2018. (in Chinese)
[47] Han L, Yao G, Tao, Z. Performance of concrete-filled thin-walled steel tubes under pure torsion. Thin-Walled Struct. 2007; 45: 24-36.
[48] Zhang Q, Liu Y, Bao Y, Jia D, Bu Y, Li Q. Fatigue performance of orthotropic steel-concrete composite deck with large-size longitudinal U-shaped ribs. Eng Struct. 2017; 150: 864-74.
[49] Wang Z, Wang J, Liu T, Zhang F. Modeling seismic performance of high-strength steel-ultra-high-performance concrete piers with modified kent-park model using fiber elements. Adv Mech Eng. 2016; 8(2): 1-14.